applied sciences

MDPI

Article

Analysis of Fractional Resonant Controllers for Voltage-Controlled Applications

Daniel Heredero-Peris [1,*], Tomàs Lledó-Ponsati [1], Cristian Chillón-Antón [1], Daniel Montesinos-Miracle [1] and Joaquim Melendez-Frigola [2]

[1] Centre d'Innovació Tecnològica en Convertidors Estàtics i Accionaments (CITCEA-UPC), Departament d'Enginyeria Elèctrica, Escola Tècnica Superior d'Enginyeria Industrial de Barcelona (ETSEIB), Universitat Politècnica de Catalunya, 08028 Barcelona, Spain; tomas.lledo@f4e.europa.eu (T.L.-P.); cristian.chillon@upc.edu (C.C.-A.); daniel.montesinos@upc.edu (D.M.-M.)

[2] Grup de Recerca en Enginyeria de Control i Sistemes Intel·Ligents (EXIT), Department d'Enginyeria Elèctrica, Electrònica i Automàtica, Institut d'Informàtica i Aplicacions, Campus Montilivi, 17003 Girona, Spain; joaquim.melendez@udg.edu

* Correspondence: daniel.heredero@upc.edu

Abstract: This paper investigates the application of fractional proportional–resonant controllers within the voltage control loop of grid-forming inverters. The use of such controllers introduces an additional degree of freedom, enabling greater flexibility in manipulating frequency trajectories. This flexibility can be harnessed to improve tracking error and enhance disturbance rejection, particularly in applications requiring precise voltage regulation. The paper conducts a conceptual stability analysis of ideal fractional proportional–resonant controllers using the Nyquist criterion. A tuning procedure based on robustness criteria for the proposed controller is also addressed. This tuning strategy is used to compare different controllers under the same conditions. In addition, a sensitivity analysis is provided, comparing the performance of fractional proportional–resonant controllers with traditional proportional–resonant controllers equipped with harmonic compensation. The controller's formulation and performance are validated through simulations and tested with a 20 kVA inverter under high non-linear loads. Compared to classical control approaches, the fractional tuning parameter enhances tracking performance, reduces phase delay, and improves disturbance rejection. These improvements are achieved with a controller designed to minimise computational demands in terms of memory usage and execution time.

Keywords: voltage control; fractional exponents; grid-forming inverters; resonant controllers

Citation: Heredero-Peris, D.; Lledó-Ponsati, T.; Chillón-Antón, C.; Montesinos-Miracle, D.; Melendez-Frigola, J. Analysis of Fractional Resonant Controllers for Voltage-Controlled Applications. *Appl. Sci.* **2024**, *14*, 10259. https://doi.org/10.3390/app142210259

Academic Editor: Giovanni Petrone

Received: 17 October 2024
Revised: 30 October 2024
Accepted: 4 November 2024
Published: 7 November 2024

1. Introduction

Regulating voltage and current in voltage source converters (VSC) is a fundamental and significant challenge. Various AC industrial applications heavily rely on effective regulation, including motor drives, parallel active filters and high-resolution AC power supplies. Multiple control strategies, such as hysteresis control, internal model control (IMC), and rotating frame control, address this issue from different perspectives [1,2].

Proportional–integral (PI) controllers and proportional–resonant (PR) controllers are commonly employed for voltage regulation. These controllers typically offer narrow bandwidth control, making them highly selective to tuned frequencies [3]. Various methods have been developed to address this limitation, such as incorporating harmonic compensators (HCs) in parallel with PI (PIHC) or PR controllers (PRHC) [4–6]. However, these methods increase complexity, computational demands, and the difficulty of tuning procedures, complicating stability/robustness analysis when multiple harmonic components need to be addressed. For example, high-frequency regulation requires phase compensation when using PRHC controllers [7,8]. Also, the tuning of the different HCs is also an object of optimal techniques [9].

Fractional calculus entered the control field in the late 1990s, though the concept of fractional order calculus (FOC) dates back to 1695 with Leibniz and l'Hôpital. FOC employs non-integer orders, including complex values, as can be seen in the non-integer compilation provided by [10], offering additional degrees of freedom for various objectives such as better modelling of complex systems or new proposal of controllers [11–13]. FOC was first applied to a PI controller in 1999 [14].

A summary table of the real order FOC formulae in different controller type adoption can be seen in Table 1 [10,15–17]. In Table 1, the orders n, λ, μ and α of controller actions are real numbers in the range of 0 and 2 (to ensure causality), the terms k_x represent the controller gains, and ω_x are angular pulsations used for tuning purposes. The promising advancements of FOC in control have led to efforts in robust tuning criteria [18,19] and dynamic enhancement [20,21].

Table 1. State of the art of the main research on non-integer controllers.

Author	Controller	Transfer Function
A. Oustaloup [10]	CRONE derivative	$k_d s^{\alpha}$
A. Oustaloup [10]	CRONE integrator	$k_i \frac{1}{s^{\alpha}}$
I. Poudlubny[14]	PI^{λ}	k_p+k_i/s^{λ}
	PID^{μ}	$k_p+k_i/s+k_d s^{\mu}$
	$PI^{\lambda}D^{\mu}$	$k_p+k_i/s^{\lambda}+k_d s^{\mu}$
M. Tenoutit [15]	$(PI)^n$	$s^{-n}(k_p+k_i/s^{\lambda})$
	$(PD)^n$	$s^{-n}(k_p+k_i s^{\mu})$
	$(PID)^n$	$s^{-n}(k_p+k_i/s^{\lambda}+k_d s^{\mu})$
Tavakoli [15]	IMC-FOPID	$k_p+k_i/s^{\alpha}+\frac{k_d s^{\alpha}}{\gamma s^{\alpha}+1}$
Luo [15]	$(PI)^{\lambda}$	$(k_p+k_i/s)^{\lambda}$
	$(PD)^{\mu}$	$(k_p+k_d s)^{\lambda}$
El-Khazali [15]	Mod-FOPID	$k_c \frac{(1+T_i s^{\mu})^2}{s^{\mu}}$
ine F. Merrikh-Bayat [15]	Non-Linear FOPID	$k_d \lvert D^{\mu}e(t)\rvert^{\beta} sign(D^{\mu}e(t))$
		$+k_i \lvert D^{\lambda}e(t)\rvert^{\gamma} sign(D^{\lambda}e(t))$
D.Heredero [16]	FPR	$k_p+k_i \frac{s^{\alpha}}{s^2+\omega_0^2}$
D. Xue [15]	Fractional Lead-Lag	$\left(\frac{1+s/\omega_b}{1+s/\omega_h}\right)^r$

In 2018, a formal translation from PR to fractional PR (FPR) controller was established [22], following an initial presentation in 2016 [23]. The FPR was later renamed as fractional ideal PR controller in 2021 [24]. Research [16,24] shows that FPR controller increases control bandwidth with a lower computational burden than PRHC controllers, though these studies primarily focus on current regulation. The study in [24] presents a stability analysis by examining the trajectory of eigenvalues, but it is still under the current control framework. From [22] to [24], it can be concluded that the fractional component helps to modify the frequency trajectory, mainly in terms of phase lead-lag manipulation.

According to the aforementioned studies, when using FPR controllers, the frequency domain response has a potential manipulation capability. This idea can be extended for applications other than controlling the current loop of VSCs. Thus, regarding voltage regulation in VSCs, several studies have explored the application of FOC to PI controllers [25,26]. For instance, the fractional use of PID in [27] demonstrates improved time response and superior disturbance rejection. However, applying FOC to PR controllers is less widespread in the voltage control framework. The study presented in [28] is one of the few examples of applying FPR to voltage regulation. Although the tuning criterion employed is based on an

optimal technique (the particle swarm optimisation (PSO) algorithm), it focuses exclusively on minimising the system error. Thus, aspects such as stability and disturbance rejection capability are not considered.

This paper seeks to extend the application of fractional proportional–resonant (FPR) controllers from AC current control to AC voltage regulation. The primary contribution is a stability analysis of ideal FPR controllers, based on the Nyquist criterion, conducted in the continuous-time domain and applied to the capacitor voltage control of a voltage source converter (VSC). Additionally, the paper proposes a method for determining the controller gains for specific fractional values of the FPR controllers based on the phase margin criterion. This controller gain tuning criterion is applied for a case study that offers a sensitivity analysis, examining the effect of selecting different fractional values for the FPR controller. The analysis also contrasts the results with the classical idea (no damped) PR and PRHC controllers. This study evaluates reference tracking capability, disturbance rejection, robustness, and the impact of modelling inaccuracies on stability margins. The results indicate that the fractional term is critical in achieving various control objectives. By selecting appropriate fractional terms, improvements in both tracking and disturbance rejection can be realised. Thus, FPR controllers offer a viable solution for high-accuracy AC voltage systems, such as AC power supplies, grid-forming converters, or series active filters. Furthermore, the paper shows that this type of controller is well suited for applications with computational constraints, particularly in terms of execution time and memory usage.

The paper layout is as follows. Section 2 introduces the system and the design considerations and develops the controller stability by applying the Nyquist criterion. Section 3 proposes the tuning strategy for the next sections. Section 4 presents and validates a control analysis based on the system sensitivity and the tolerable modelling uncertainty. Section 5 shows the experimental tests. Section 6 presents a discussion the results. Finally, in Section 7 we draw the conclusions.

2. Nyquist Analysis for Ideal FPR Controller on Voltage Applications

This section presents the design control considerations, details the ideal voltage FPR formulation and analyses its stability using the Nyquist trajectory. Although Matignon's theorem [29] is explicitly oriented to stability analysis of fractional order systems, it has not been considered. Nyquist criterion exposes a wider applicability (valid for fractional and integer systems). It also offers a more intuitive approach for feedback system stability analysis while giving insight into gain margins and phase margins. Thus, the Nyquist criterion can detect the robustness and margins of stability more easily than Matignon's theorem.

2.1. Initial System Considerations

The purpose of grid-forming inverters is to generate a stable and robust voltage.

Figure 1 shows the used schematic for a voltage-controlled voltage source converter (VC-VSC). An inductive (L)–capacitive (C) output coupling filter interfaces the inverter with the AC side. The VC-VSC control is based on two nested control loops. The inner loop regulates the current (i_l) through the inductance L, and the outer loop controls the output capacitor's voltage (v_c) using i_l. The capacitor includes an equivalent series resistance (ESR), (r_C). This r_C only considers the parasitic resistance of the capacitor to allow a more realistic model. Thus, the capacitor voltage is

$$V_c(s) = \frac{Cr_C s + 1}{Cs} I_l(s). \tag{1}$$

As an assumption, the inner current control loop is considered pre-tuned, with enough bandwidth and adequate time response to avoid cross-coupling effects [30]. Thus, the inner control loop is considered as a unitary gain in the following analysis.

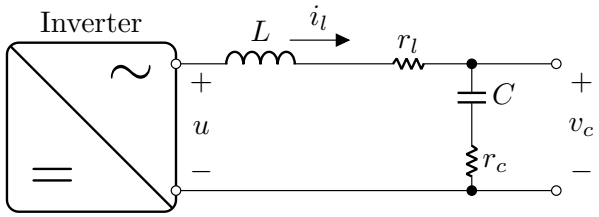

Figure 1. Voltage-controlledvoltage source converter (VC-VSC) schematic with inductive (*L*)–capacitive (*C*) filter.

The FPR formulation considered in this paper follows [23]

$$G_{\mathrm{FPR}}(s) = k_{\mathrm{p}} + k_{\mathrm{i}} \frac{\omega_0 s^{\alpha}}{s^2 + \omega_0^2}. \tag{2}$$

In (2), the α value is the fractional-order value $\{\alpha \in (0, 2]; \alpha \in \mathbb{R}\}$, ω_0 is the resonant angular speed, and k_{p} and k_{i} are the proportional and integral gains, respectively. The α value is not considered negative as the studied behaviour is moved from a fractional derivative response to an integral one. In the same direction, values higher than two involve non-causal controllers. Note that when α is one, (2) results in a classical ideal PR controller.

Considering (1) and (2), the open-loop transfer function is

$$G_{\mathrm{ol}}(s) = \frac{Cr_C s + 1}{Cs} \left(k_p + k_i \frac{\omega_0 s^{\alpha}}{s^2 + \omega_0^2} \right). \tag{3}$$

Consequently, the closed-loop transfer function results

$$G_{\mathrm{cl}}(s) = \frac{V_c(s)}{V_c^*(s)} = \frac{\frac{Cr_C s+1}{Cs} \left(k_p + k_i \frac{\omega_0 s^{\alpha}}{s^2+\omega_0^2} \right)}{1 + \frac{Cr_C s+1}{Cs} \left(k_p + k_i \frac{\omega_0 s^{\alpha}}{s^2+\omega_0^2} \right)} \tag{4}$$

where the super-index $*$ designs to the reference signal.

Once (3) and (4) are obtained, it would be interesting to gain an initial insight into the effect of the α parameter when applied to the voltage control of the capacitor *C*. Thus, for computations, and without loss of generality, it will be considered a real system with specific parameters as a case study.

Table 2 summarises the base system parameters.

Table 2. Base plant and controller parameters.

Parameter	Descriptor	Value	Unit
C	Capacitance	75	µF
L	Inductance	492	µH
r_C	Capacitor ESR	8	mΩ
r_l	Inductor ESR	50	mΩ
k_{p}	Proportional gain	0.0494	
k_{i}	Integral gain	0.0363	

Figure 2 and Figure 3 show the Bode diagram for $G_{\mathrm{ol}}(s)$ and $G_{\mathrm{cl}}(s)$, respectively.

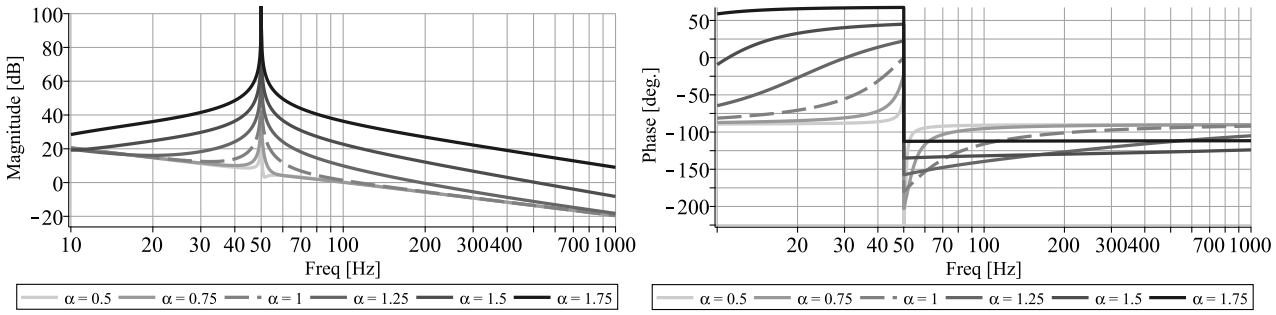

(**a**) Magnitude (**b**) Phase

Figure 2. Open−loop (G_{ol}) bode diagrams, based on Table 2.

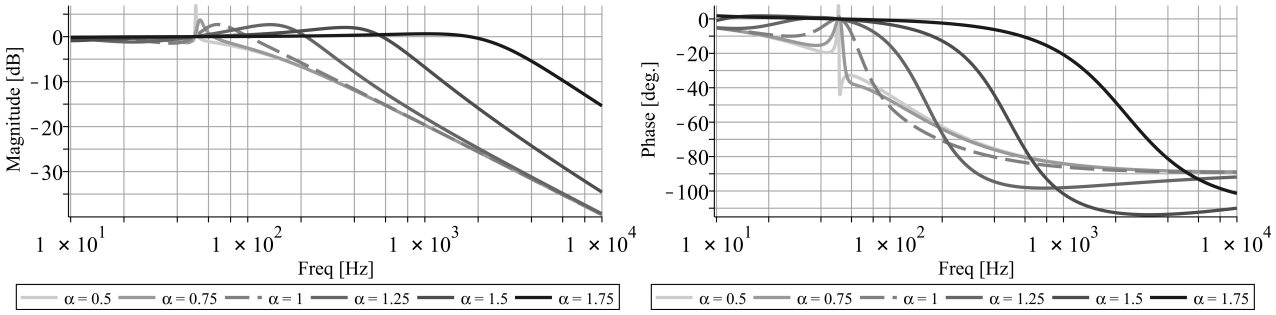

(**a**) Magnitude (**b**) Phase

Figure 3. Close−loop (G_{cl}) bode diagrams, based on Table 2.

Analysing Figure 2a it can be observed that α values above 1 contribute to an $G_{ol}(s)$ with higher gains outside ω_0. This effect is translated to the $G_{cl}(s)$ behaviour extending the bandwidth, refer to Figure 3a. On the contrary, α values below 1 result in increased selectivity. Furthermore, Figure 2b shows that at frequencies above ω_0, it reduces faster its phase. This is translated into a $G_{cl}(s)$ with the worst tracking capability near ω_0, but with the same phase delay for higher frequencies. So, there is room for this selective behaviour of the FPR with α values below 1 to be useful in the function of the implementation design and its tuning procedure.

2.2. Stability Analysis Based on a Conceptual Nyquist Trajectory

It is possible to rewrite (2) in the frequency domain by using

$$(\mathrm{I}\omega)^{\alpha} = \omega^{\alpha} e^{\left(\frac{\mathrm{I}\pi\alpha}{2}\right)} \tag{5}$$

obtaining

$$G_{\mathrm{FPR}}(\mathrm{I}\omega) = \frac{k_p(-\omega^2 + \omega_0^2) + k_i\omega_0\omega^{\alpha}e^{\left(\frac{\mathrm{I}\pi\alpha}{2}\right)}}{-\omega^2 + \omega_0^2}. \tag{6}$$

Assuming that the valid α range is (0, 2] (causal order controllers), it can be deduced that there are three significant frequencies on the Nyquist diagram expressed in (3) and (6); the starting point of the trajectory (ω = 0), the behaviour in the neighbourhood of the resonant frequency ($\omega = \omega_0$), and the ending point ($\omega = \infty$). The study of these significant frequency values, their vicinity limits and the real-axis potential cross points provides a close idea of how to depict the Nyquist trajectory conceptually. Thus, the stability can be deduced.

To facilitate the Nyquist trajectory analysis, the real and imaginary parts of (3) are decoupled as $\mathbb{R}\{G_{ol}(\mathrm{I}\omega)\}$ by

$$\frac{k_i\omega_0\omega^{\alpha}\left(-C\omega\cos\left(\frac{\pi\alpha}{2}\right) - \sin\left(\frac{\pi\alpha}{2}\right)\right) + k_p r_c C(\omega^3 - \omega\omega_0^2)}{\omega C(\omega^2 - \omega_0^2)} \tag{7}$$

and the $\mathbb{I}\{G_{ol}(\mathrm{I}\omega)\}$ by

$$\frac{k_i\omega_0\omega^{\alpha}\left(-\omega r_C C\sin(\frac{\pi\alpha}{2})+\cos(\frac{\pi\alpha}{2})\right)+k_p(-\omega^2+\omega_0^2)}{\omega C(\omega^2-\omega_0^2)}, \tag{8}$$

respectively. In this sense, the analysis shown in (7) and (8) drives to:

2.2.1. $\omega = 0$ (Starting Point)

$\forall\ \alpha$, the starting point is $(r_c k_p, -\infty\mathrm{I})$ in the complex Nyquist's plane. It can also be deduced that the limit of ω to the positive vicinity ($\omega \to 0^+$) suits the starting point.

2.2.2. $\omega = \omega_0$ (Resonance Point)

This value is critical to understanding how the Nyquist trajectory evolves. At $\omega = \omega_0$ an indeterminate form of the type $0/0$ can be found. Analysing the slope at this point, it corresponds to the ratio $\frac{\mathbb{I}\{G_{ol}(I\omega)\}}{\mathbb{R}\{G_{ol}(I\omega)\}}$, yielding to

$$\frac{-\cos(\frac{\pi\alpha}{2})-\omega_0 r_C C\sin(\frac{\pi\alpha}{2})}{\sin(\frac{\pi\alpha}{2})-\omega_0 r_C C\cos(\frac{\pi\alpha}{2})}. \tag{9}$$

From (9), obtaining specific values for specific α proposals is possible. Thus, the slope is reduced to $\omega_0 r_C C$ for the case $\alpha = 1$, while for the extreme range values (0 and 2) the slope responds to $-1/(\omega_0 r_C C)$.

2.2.3. $\omega = \infty$ (End Point)

The Nyquist trajectory always ends in the real axis being null and the imaginary part $\forall\ \alpha$ being in the analysed interval. However, the real part, $\mathbb{R}\{G_{ol}(I\omega)\}|_{\omega=+\infty}$, has different ending values depending on α,

$$\begin{cases} r_C k_p & \forall\alpha \in [0,2) \\ r_C\left(k_i\omega_0 + k_p\right) & \text{for } \alpha = 2. \end{cases} \tag{10}$$

2.2.4. Crosspoints with Real Axis

The possible crossing points with the real axis are required to obtain the stability from the Nyquist criterion (detect number of encirclements of $(-1,0\mathrm{I})$). For integer α values, it is possible to obtain exact crossing points.

- For α = 0, the crossing point with the real axis takes place at (0,0I) when the ω is $\pm\frac{\sqrt{k_p\omega_0(k_p\omega_0+k_i)}}{k_p}$.
- For α = 1, the crossing point takes place at ($\frac{r_C^2C^2k_p\omega_0^2+r_CCk_i\omega_0+k_p}{r_CC^2\omega_0^2}$,0I) when the ω is $\pm\frac{\sqrt{(r_CCk_i\omega_0+k_p)k_p}\omega_0}{r_CCk_i\omega_0+k_p}$.
- For α = 2, the crossing point takes place at (0,0I) when the ω is $\pm\frac{\sqrt{(\omega_0k_i+k_p)k_p}\omega_0}{\omega_0k_i+k_p}$.

The other crossing points for $\alpha \in (0,2)\backslash\{1\}$ values are not analytically possible due to the roots from (8) as a function of the ω requires the resolution of a transcendental equation. Thus, the exact values of the crossing points for all the other intermediate values of α require the setting of the parameters (k_p, k_i, r_C, C and ω_0). It has been proposed to analyse numerically possible crossing points for ω_0 equal to 100π rad/s (50 Hz), $k_p \in [0,100]$, $k_i \in [0,10,000]$, $r_C \in [0,100]$ mΩ, $C \in [0,1]$ mF and $\alpha \in (0,2)\backslash\{1\}$. The frequency of 50 Hz is selected as it corresponds to the typical AC rated frequency for Europe, Asia, Africa, and Australia. The same qualitative results arise if 60 Hz is used instead. All previous intervals are split into 100 points except for the α, which is split into 10 values. Then, 10^{10} different cases were numerically evaluated, concluding that for intermediate α, only one crossing point is present for $\omega \in (0,\infty)$.

2.2.5. Nyquist Curve Drawing Considerations

This section describes the assumptions or considerations made for all the non-analytically attainable results from previous sections.

- In terms of the slope near the resonance frequency. Thus, assuming reasonable r_C and C values, i.e., $r_C C \approx 10^{-6} - 10^{-9}$, it can be analysed that from $\alpha = 0$ to 1, the slope starts from being huge and negative, to decrease its slope until the negative vicinity side of $\alpha = 1$. There is a discontinuity at that point, and the slope abruptly goes from negative to $\omega_0 r_C C$. From $\alpha = 1$ to 2, the slopes increase again to the extreme case ($\alpha = 2$) where another discontinuity goes to $-1/(\omega_0 r_C C)$.
- In terms of crossing points. When α moves from 0 to 1 (not included), the cross point is moving from (0,0I) to ($-x$,0I), with x being the exact real part of the crossing point. Then, at α equal to 1, there is an abrupt change, and the cross-point is positive and equal to $(\frac{r_C^2 C^2 k_p \omega_0^2 + r_C C k_i \omega_0 + k_p}{r_C C^2 \omega_0^2}, 0I)$. Now, from α equal to 1 to 2 (not included), the cross-point is (x,0I), where x reduced its value until 0 when α equals exactly 2.

2.2.6. Analysis

The following sections collect all previous results (Sections 2.2.1–2.2.5) for the case of using the FPR controller for voltage applications. It should be noted that the analysis is valid when the voltage loop is not affected by any inner loop and the controller is implemented in the continuous-time domain.

The conceptual Nyquist trajectories are illustrated in Figure 4. In this figure, the solid lines represent the conceptual trajectory of the Nyquist curve. In contrast, the dashed lines serve merely as supporting elements to aid in understanding the asymptotic behaviour of the resonance when the frequency ω approaches ω_0.

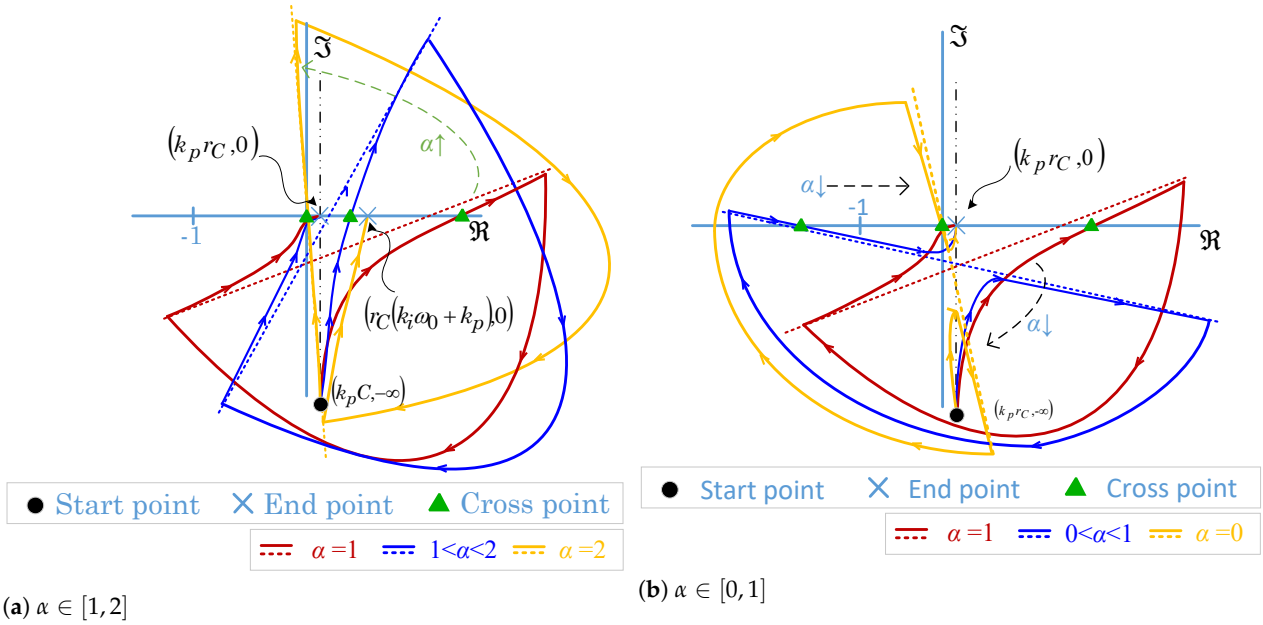

(**a**) $\alpha \in [1, 2]$ (**b**) $\alpha \in [0, 1]$

Figure 4. Conceptual Nyquist trajectories for $\alpha \in [0, 2]$ (solid lines define the Nyquist trajectory, and dashed lines describe asymptotic behaviours).

It can be seen that the stability is potentially ensured independently of the controller gains for any α value above 1. This is because no encirclement of (-1,0I) is present, and (3) does not have poles with positive real parts. On the contrary, below 1, there is a point where the system becomes unstable. In other words, according to the selected α and system parameters (controllers gains and system values), the system stability is compromised. In fact, small α values will tend to create a crossing point at the right of (-1,0I), yielding to two clockwise encirclements of (-1,0I). But, if the α is big enough but still lower than 1,

the crosspoint will be moved to the left of (−1,0I). This fact supposes one clockwise and one anti-clockwise encirclement of (−1,0I). The result is a stable system.

Regarding stability margins, it is complicated to provide a qualitative analysis due to the intrinsic asymptotic behaviour of the FPR controller. Thus, it will be treated in the following sections.

3. Tuning the Voltage FPR

This section aims to propose a tuning procedure for the voltage FPR. A procedure was proposed in [16] based on a standard PR controller tuned with time domain specifications. Thus, ref. [16] relies in different Bode diagrams considering different α values. So, the final decision turns to the frequency domain curves. In [28], the tuning criterion uses an optimal technique (the particle swarm optimisation (PSO) algorithm) to obtain the gains for a specific pre-selected α value. This paper proposes an alternative method to face the system's robustness.

3.1. Tuning Method Based on Phase Margin Selection

This procedure is based on choosing the controller in the function of phase margin specifications. Thus, it builds on robustness criteria. All the possible controllers (considering different α values) will have the same bandwidth at a specified design frequency. So, the proposed steps to tune the controller are:

Step 1. Select the system specifications. It is used to choose the desired phase margin value, ϕ_m, for the controller at a specified gain-crossover frequency, ω_c.

Step 2. Tune a set of different proportional and integral k_p-k_i gains for a desired ϕ_m and different α values from 0 to 2. In [31] ϕ_m at ω_c can be defined as

$$G_C(\mathrm{I}\omega_c)G(\mathrm{I}\omega_c) = e^{-\mathrm{I}(\pi-\phi_m)} = -\cos(\phi_m) - \mathrm{I}\sin(\phi_m) \tag{11}$$

where $G_C(\mathrm{I}\omega_c)$ and $G(\mathrm{I}\omega_c)$ are the isochronous transfer functions of the controller and the plant, respectively. Applying (1) and (2) to (11), the k_i gain is

$$\frac{C(\sin(\phi_m)r_C\,C\,\omega_c + \cos(\phi_m))\left(\omega_c^2 - \omega_0^2\right)\omega_c^{-\alpha}}{\left(C^2r_C^2\omega_c^2 + 1\right)\omega_0\cos\left(\frac{\pi\alpha}{2}\right)} \tag{12}$$

and the k_p gain results

$$-\frac{C\omega_c\left((\cos(\phi_m)r_C\,C\,\omega_c - \sin(\phi_m))\cos\left(\frac{\pi\alpha}{2}\right) + (\sin(\phi_m)r_C\,C\,\omega_c + \cos(\phi_m))\sin\left(\frac{\pi\alpha}{2}\right)\right)}{\left(C^2r_C^2\omega_c^2 + 1\right)\cos\left(\frac{\pi\alpha}{2}\right)} \tag{13}$$

Step 3. Decision stage. Depict the different Bode plots for the different α values. As all the plots have the same ϕ_m, choose the more suitable one for the system application regarding excitation region, bandwidth or delay at some strategic frequency tones.

3.2. Implementation and Validation

After applying a tuning method, the designer will have at least one set of k_p, k_i and α variables to evaluate.

Step 4. Look for an accurate approximation to the s^α term that makes the controller's non-integer part implementable. Various authors study this problem, proposing different approaches [32–34]. In [16], a comparison is applied to FPR controllers, determining that Charef's approximation proposed in [32] is one of the best alternatives.

Step 5. Check the Step 4 validity. A comparison of robustness and sensibility should be conducted.

Step 6. Check the correct tracking response by simulations, paying special attention to voltage tracking and disturbance rejection capability.

3.3. Applying of the Tuning Procedure

This section illustrates the tuning procedure that was previously detailed. It will be considered as ω_0 set at 100π rad/s (50 Hz). The inner control loop is assumed to have a bandwidth of 3000 Hz. Thus, the different steps are detailed in the following Sections 3.1 and 3.2.

Step 1. For robustness purposes, it is recommended a phase margin, ϕ_m, value of 60°. This ϕ_m will be set at ω_c = 500 Hz (this fact allows to avoid cross-coupling between inner and outer control loops).

Step 2. Table 3 shows the obtained set of values for $\alpha \in [0.5, 1.5]$ applying (12) and (13).

Step 3. This step allows for comparing the different ideal open-loop Bode diagrams to make a decision (no approximation used for the term s^{α}).

Table 3. Controller gains values, obtained from (12) and (13), considering ϕ_m = 60° and ω_c = 500 Hz.

α	k_p	k_i	α	k_p	k_i
0.5	0.4507	215.71	1.25	0.2172	0.3057
0.75	0.3540	20.273	1.5	0.1204	0.0490
1	0.2856	2.2999			

In Figure 5, it can be seen how the ϕ_m is 60° at 500 Hz $\forall\alpha$. This is also reflected in the close loop Bode diagram in Figure 6. Due to this tuning procedure, the α exponent is relegated to be selected for a better gain or phase delay tracking enhancement. It should be noted that when this criterion is applied α values below 1 offer an overall better tracking response. The opposite conclusion was obtained compared with Figure 3. In Figure 3, the gains are kept equal between the compared controllers. Thus, stability margins are delegated to this decision.

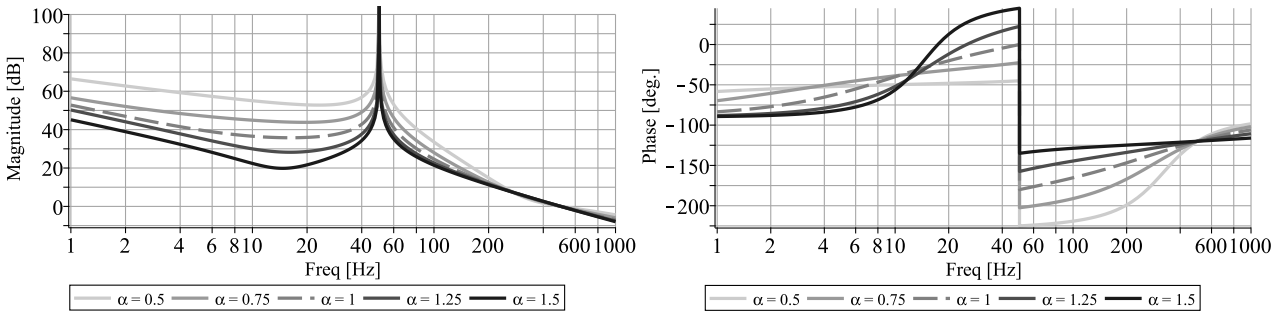

(**a**) Magnitude diagram. (**b**) Phase diagram.

Figure 5. Open−loop bode diagrams for ideal FPR controller, based on Table 3.

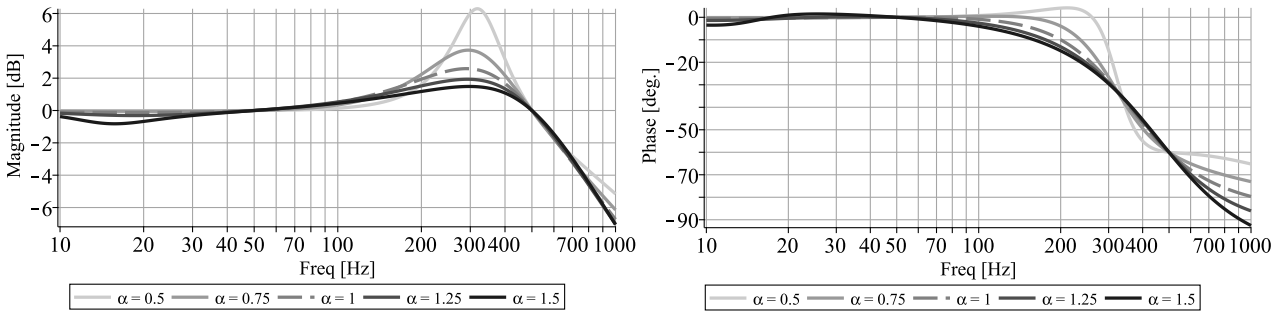

(**a**) Magnitude diagram. (**b**) Phase diagram.

Figure 6. Close−loop bode diagrams for ideal FPR controller, based on Table 3.

Step 4. Following Charef's approximation described in [16], it is required to set the corresponding Charef's approximation parameters. For clarity and ease of comparison with PR and PRHC, only $s^{0.75}$ and $s^{1.5}$ are approximated. Thus, for both α cases, the Charef's

parameter p_T is set to 1 (filter coefficient). The other Charef's parameters are set to y = 3.5 dB (maximum deviation between ideal and approximated curve) and n = 2 (approximation order) to approximate $s^{0.75}$t, and y = 4 dB and n = 3 to approximate $s^{1.5}$.

Step 5 and 6. The detailed analysis of the robustness and stability is addressed in Section 4.

4. Control Analysis Based on Sensitivity

A sensitivity analysis is performed in this section. This paper is focused on the sensitivity, $S(s)$, the complementary sensitivity, $T(s)$, and the input sensitivity, $S_i(s)$, for the reference tracking, disturbance rejection, and robustness study. Note that $S(s)$ is defined as

$$\frac{1}{1+G_C(s)G(s)}, \tag{14}$$

$T(s)$ as

$$\frac{G_C(s)G(s)}{1+G_C(s)G(s)}, \tag{15}$$

and $S_i(s)$ as

$$\frac{G(s)}{1+G_C(s)G(s)}. \tag{16}$$

For simplicity purposes, the analysis compares four different controllers: (i) FPR with α = 0.75; (ii) FPR with α = 1.5; (iii) FPR with α = 1 (PR controller); and finally (iv) PRHC based on (iii) with a third and fifth HC. The plant parameters are listed in Table 2. The controllers gains have been presented in Section 3. The HC gains are obtained by the fundamental integral gain scaling it by the harmonic component.

4.1. Reference Tracking

$S(s)$ can be used to assess the reference tracking performance quantitatively. The error dynamic behaviour, $\varepsilon(s)$, in the absence of any other input rather than the reference $R(s)$, can be defined as

$$\varepsilon(s) = R(s) - Y(s) = \cdots = S(s)R(s) \tag{17}$$

where $Y(s)$ designates the transfer function of the time-dependent output magnitude defined by $y(t)$. Unfortunately, the final value theorem used to analyse the steady-state error from $S(0)$ is not feasible. This is due to the pure imaginary poles of a sinus signal reference.

The error tracking study is then delegated to the complementary sensitivity, $T(s)$, i.e., to the close-loop response. Figure 7 compares the close-loop bode diagram for PR, PRHC (with third and fifth harmonic compensators) and FPR controllers. In this figure, the green line illustrates the current inner loop bode diagram, denoting that it has enough bandwidth to avoid relevant cross-coupling effects between control loops. It can also be seen that all three controllers present close design ϕ_m at ω_c although the s^α term has been approximated according to Section 3-step 4. Also, in Figure 7a, it can be observed that the α value modifies the behaviour of the gain tracking, being the controller with α = 0.75 the worst one (wider excitation region) and α = 1.5 the best one. However, Figure 7b shows that α = 0.75 results in better phase tracking. Paying attention to the PRHC case, it can be concluded that it is better at tuning harmonic components, but it produces a cross-coupling effect, and the excitation regions are extended.

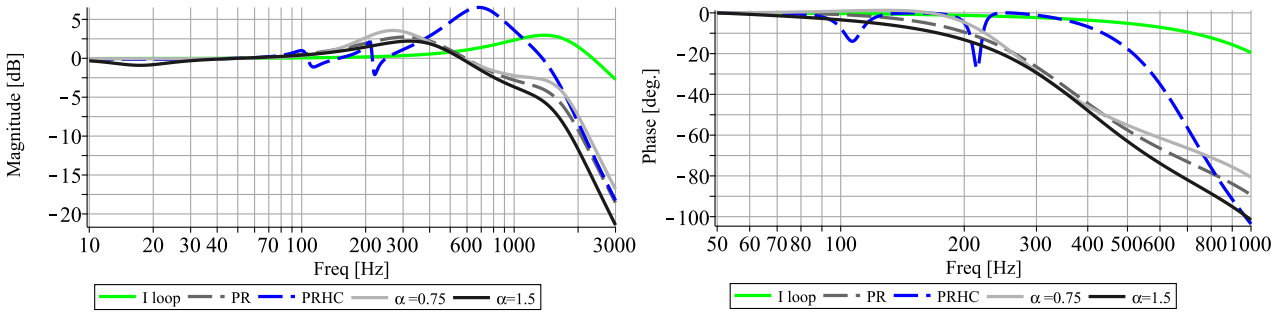

(**a**) Magnitude diagram. (**b**) Phase diagram.

Figure 7. Close−loop bode ($T(s)$) diagrams for the controller selection comparison.

4.2. Input Disturbance Rejection

The open-loop transfer function, G_{ol}, and the close-loop transfer function, G_{cl}, are related by the sensitivity transfer function as

$$Y_{cl}(s) = S(s)Y_{ol}(s). \tag{18}$$

Thus, (18) is valid when any entry except the main reference produces the excitation. This means that $S(s)$ provides information about the attenuation offered by the feedback inclusion. However, the input sensitivity, $S_i(s)$, explicitly analyses the disturbance effect of an input disturbance on the system's output variable.

Figure 8 depicts the bode diagram for $S_i(s)$, concluding that the controller with α value of 0.75 better rejects the disturbances with frequencies in the vicinity of ω_0. On the contrary, α = 1.5 has the worst rejection capabilities.

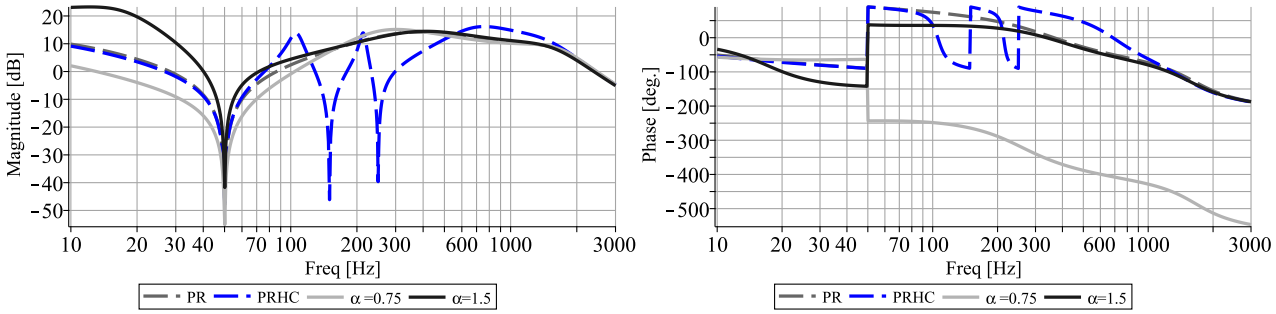

(**a**) Magnitude diagram. (**b**) Phase diagram.

Figure 8. Input sensitivity ($S_i(s)$) bode diagrams for the controller selection comparison.

4.3. Robustness

The stability and robustness are analysed using the Nyquist trajectory defined as

$$L(\mathrm{I}\omega) = G_C(\mathrm{I}\omega)G(\mathrm{I}\omega) \tag{19}$$

where ω is the pulsation. Furthermore, adding 1 to (19) yields to $S(\mathrm{I}\omega)^{-1}$. Hence, it can be deduced that the stability is closely related to the sensitivity transfer function, $S(s)$. In fact, the minimum distance from the point (−1,0I) to the Nyquist trajectory, α_s, matches the inverse of the maximum level of sensitivity defined as [35]

$$\mathrm{M_s} = \max_{\omega} |S(\mathrm{I}\omega)| = \frac{1}{\alpha_s}, \tag{20}$$

to consider the system as robust, a M_s value below 2 p.u. is recommended by [36]. Furthermore, (20) provides more conservative but also more concise information about stability than GM and PM [37]. This yields to

$$\begin{aligned} \mathrm{GM}^* &= \frac{1}{1-\alpha_s} \\ \mathrm{PM}^* &= 2\arcsin\left(\frac{\alpha_s}{2}\right) \end{aligned} \tag{21}$$

where the superscript * denotes an alternative to GM or PM.

Figure 9 outlines the ending part of the Nyquist trajectory for the case under study.

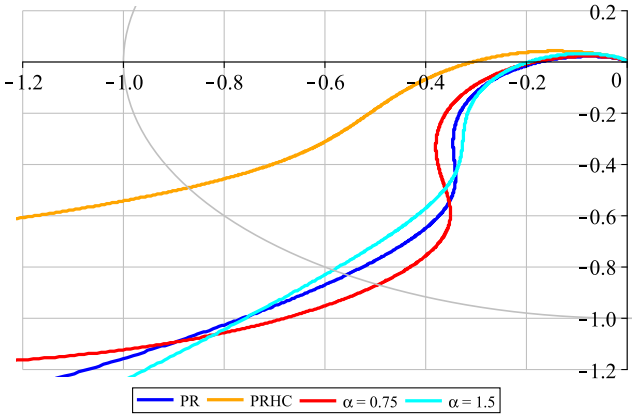

Figure 9. Nyquist of $L(\mathrm{I}\omega)$ ending trajectory. Grey line defines the unitary circle for discrete−time systems.

From Figure 9, it is possible to obtain Table 4. Note that $f_{\mathrm{M_s}}$ represents that frequency where M_s occurs. Evaluating the results, both PR and FPR options present similar robustness, but the PRHC exhibits worse values.

Table 4. Tuned stability parameters, based on controller gains from Table 3.

α	f_{Ms} (Hz)	M_s (dB)	Ms	α_s	GM	PM (°)	GM *	PM * (°)
PRHC	987.7	3.375	1.475	0.678	17.67	40.097	3.11	39.634
0.75	3009.9	2.231	1.293	0.773	18.96	54.719	4.41	45.504
1	2798.6	1.979	1.256	0.796	19.71	55.997	4.91	46.922
1.5	1965.6	2.071	1.269	0.788	18.42	56.247	4.71	43.99

Superscript * denotes alternative gain and phase margin defined by (21).

4.4. Inaccuracies on Modelling

Modelling inaccuracies can result in instability problems. For this purpose, the additive uncertainty, $\Delta G(s)$, and the multiplicative uncertainty, $\delta G(s)$, are usually considered. Thus, part of the robust stability problem can be applied:

$$\frac{|\Delta G(s)|}{|\,G(s)|} = |\delta G(s)| < \frac{1}{|T(s)|}. \tag{22}$$

Conducting a similar analysis as the one in Section 4.3, it is possible to define the maximum tolerable uncertainty as

$$\mathrm{M_t} = \max_{\omega} |T(\mathrm{I}\omega)| = \max_{\omega} \frac{C(\mathrm{I}\omega)G(\mathrm{I}\omega)}{1 + C(\mathrm{I}\omega)G(\mathrm{I}\omega)}. \tag{23}$$

In this case, (23) concerns the complementary sensitivity function $T(s)$ instead of $S(s)$. For this reason, the controller plays a relevant role in the stability and robustness of the system.

Table 5 summarises, in the system's worst case, the maximum admissible pure variation at the plant $G(s)$ in terms of gain, ΔG_{Mt}, and in terms of phase, ΔP_{Mt}. The results show that FPRs with α values above 1 are better in terms of ΔG_{Mt} and ΔP_{Mt} than a standard PR controller.

Table 5. Tuned uncertainty parameters, based on Table 3.

α	M_t (dB)	M_t	ΔG_{Mt} (%)	ΔP_{Mt} (°)
PRHC	4.61	1.7	21.7	12.45
0.75	4.19	1.62	23.9	13.71
1	2.71	1.366	36.9	21.26
1.5	1.78	1.227	56.2	32.63

Figure 10 represents the gain bode diagram's superior limit for the multiplicative (ΔG) and additive (δG) uncertainties, respectively. The figure shows the upper limits of ΔG and δG, concluding that up to 350 Hz, all options are similar. Still, from 350 Hz, the controller with the best plant variation tolerance is the FPR with α = 1.5, either in terms of ΔG_{Mt} and ΔP_{Mt}, and the PRHC is the one with the worst tolerance.

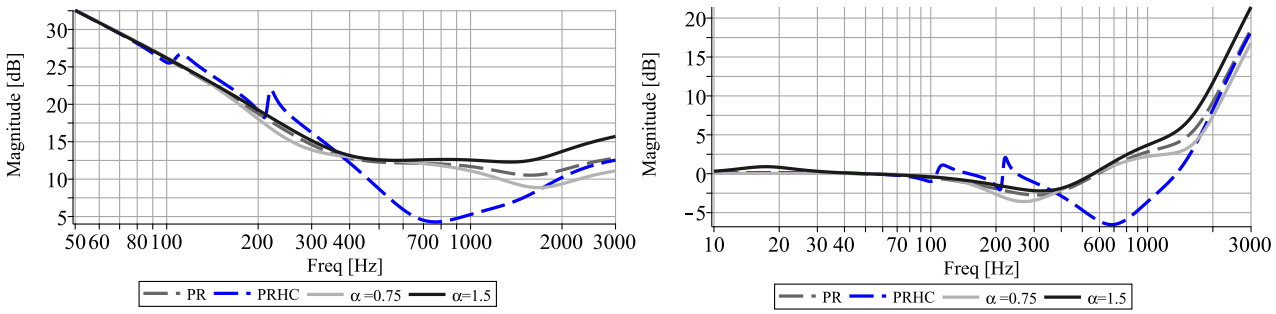

(**a**) $G(s)/T(s)$ (related with additive uncertainty ΔG) (**b**) $1/T(s)$ (related with multiplicative uncertainty δG)

Figure 10. Uncertainties' superior thresholds.

4.5. Validation

A set of simulations are performed to validate the previous analysis. Two configurations are considered. Firstly, an open-circuit configuration is evaluated to analyse the controller's performance in optimal conditions. Secondly, the controlled voltage is disturbed by different harmonic current components.

Figures 11 and 12 show the error time evolution under different voltage references with no load. This voltage reference is set to be $v_c(t) = 1\sin(h100\pi t)$ considering different harmonics components (with h being the corresponding first, second, third, and eleventh harmonic component). It can be deduced that PRHC is better at regulating the harmonic frequencies designed for (third and fifth); refer to Figure 12b. Out of these specific tones, the FPR with α below 1 is the best option.

Figure 13a–d show the regulated voltage time response when a current disturbance at different frequencies (first, second, third, and eleventh harmonics component) is applied. No feedforward is considered for the disturbance rejection analysis, and the disturbance is set to 1 A peak. Any controllers under consideration can reject the disturbance significantly, but the FPR with α = 0.75 is faster and responds to the option that excites the disturbance the least. Thus, in terms of comparison, the FPR with α below 1 is the best option for rejection.

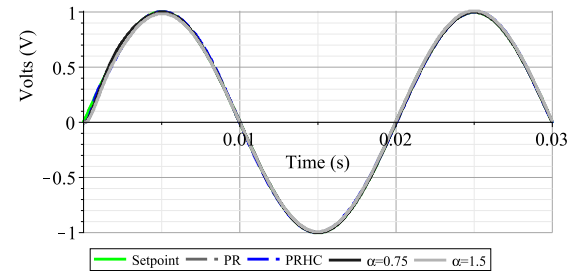

(**a**) $v_L^* = \sin(\omega_0 t)$

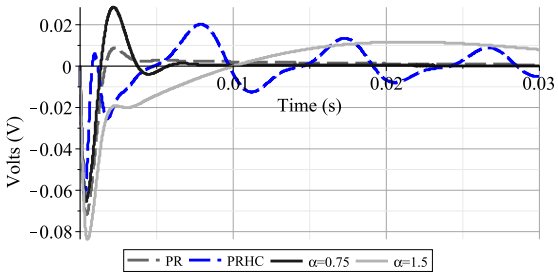

(**b**) Error tracking $v_L^* = \sin(\omega_0 t)$

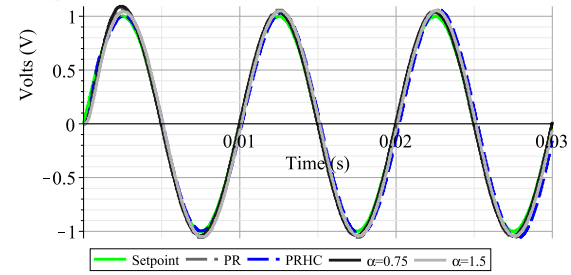

(**c**) $v_L^* = \sin(2\omega_0 t)$

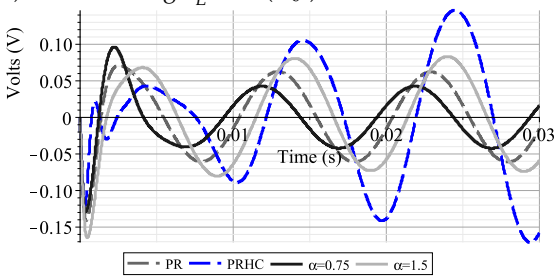

(**d**) Error tracking $v_L^* = \sin(2\omega_0 t)$

Figure 11. Time−response comparison when different references are present, being $\omega_0 = 100\pi$ rad/s (50 Hz). Harmonics 1 and 2.

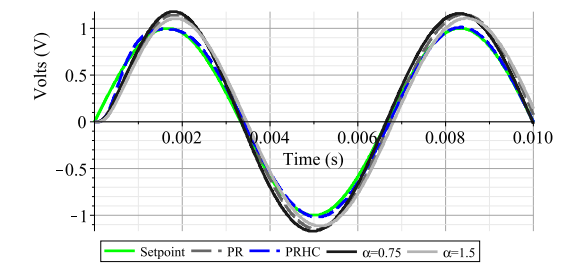

(**a**) $v_L^* = \sin(3\omega_0 t)$

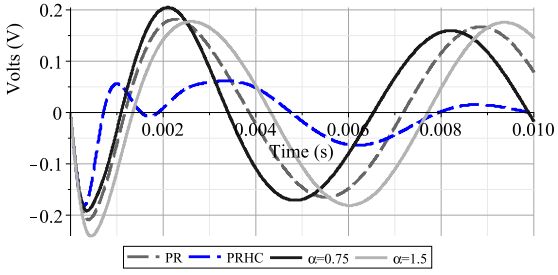

(**b**) Error tracking $v_L^* = \sin(3\omega_0 t)$

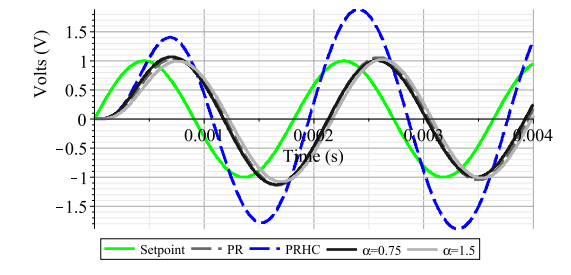

(**c**) $v_L^* = \sin(11\omega_0 t)$

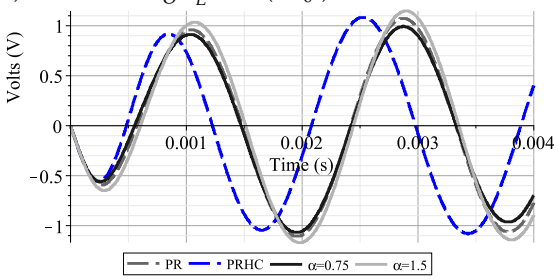

(**d**) Error tracking $v_L^* = \sin(11\omega_0 t)$

Figure 12. Time−response comparison when different references are present, being $\omega_0 = 100\pi$ rad/s (50 Hz). Harmonics 3 and 11.

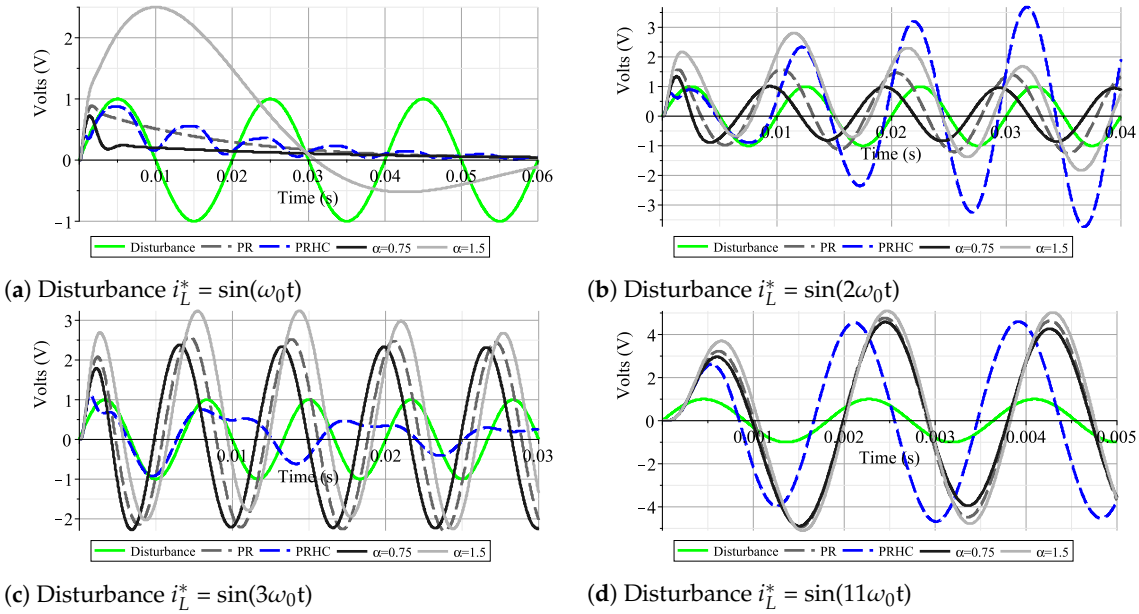

(**a**) Disturbance $i_L^* = \sin(\omega_0 t)$ (**b**) Disturbance $i_L^* = \sin(2\omega_0 t)$

(**c**) Disturbance $i_L^* = \sin(3\omega_0 t)$ (**d**) Disturbance $i_L^* = \sin(11\omega_0 t)$

Figure 13. Time−response comparison when different harmonic disturbances are present, being $\omega_0 = 100\pi$ rad/s (50 Hz).

5. Experimental Results

This section presents the different controllers' implementation in Section 4. They have been implemented in a DSP F28M36 from Texas Instruments (headquartered in Dallas, TX, USA) at 30 kHz. The inverter used is a full SiC 20 kVA device.

It can be seen in Figure 14. The experimental parameters are the same as in Table 2. The experimental plots' data have been captured with a DL9040 Yokogawa oscilloscope (headquartered in Tokyo, Japan) at 1.25 MHz and depicted by Matlab v.2024a (headquartered in Natick, MA, USA). Two different scenarios are considered, being consistent with the study cases in Section 4.5: open-circuit configuration and operation under non-linear load. For implementation purposes, the system proposed in (1) is discretised by the zero-order hold method. Then, each controller approximation obtained by Charef in Section 3 is moved to the discrete-time domain using the Tustin transformation, as suggested in [16].

Figure 14. VSVC power converter.

5.1. Open-Circuit Configuration

The open-circuit configuration case validates the simulation results obtained in Figures 11 and 12. A multi-harmonic reference voltage is added to a 325 V at the 50 Hz

setpoint. The setpoint considers 16 V at 150 Hz, 11 V at 250 Hz, 6 V at 350 Hz and 2 V for 450 and 550 Hz.

Figure 15 shows the results. Figure 15a,b show the transient and error time response when the setpoint changes to the specified multi-harmonic voltage. The Fast Fourier Transform (FFT) is also computed for both the setpoint reference and the error.

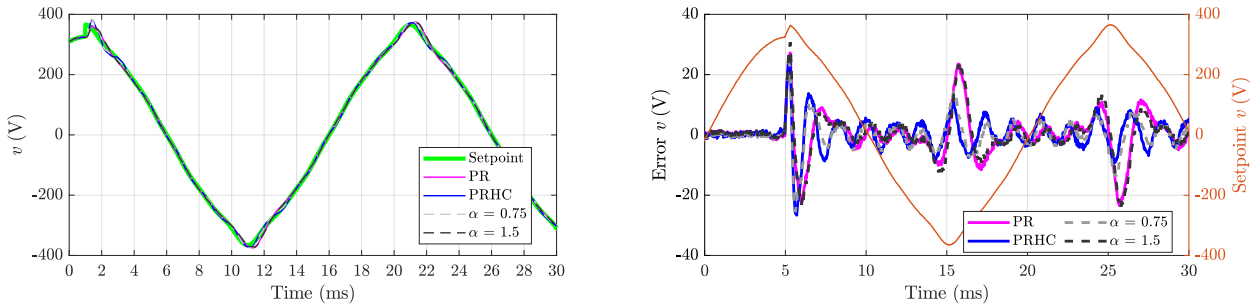

(**a**) Voltage tracking (**b**) Voltage tracking error

Figure 15. Tracking voltage time response. The orange line in the right figure depicts the voltage reference on the tracking error plot.

Table 6 provides specific values and highlights the best option for each component.

Table 6. Multi-harmonic setpoint response for all four controllers.

Controller	V_{150Hz} (V/V)	V_{250Hz} (V/AV)	V_{350Hz} (V/V)	V_{450Hz} (V/V)	V_{550Hz} (V/V)
PR	1.393	1.389	1.396	1.189	1.060
PRHC	**1**	**1**	**1.270**	1.673	2.254
$\alpha = 0.75$	1.067	1.197	1.372	1.546	1.929
$\alpha = 1.5$	1.128	1.278	1.322	**1.213**	**1.004**

Bold values indicate the best option.

From Figure 16 and Table 6, it can be concluded that PRHC is better at its tuned frequencies (third and fifth), but the FPR starts to improve or to be equivalent from the fifth harmonic onwards according to the selected α value. The same result is derived from Section 4.5.

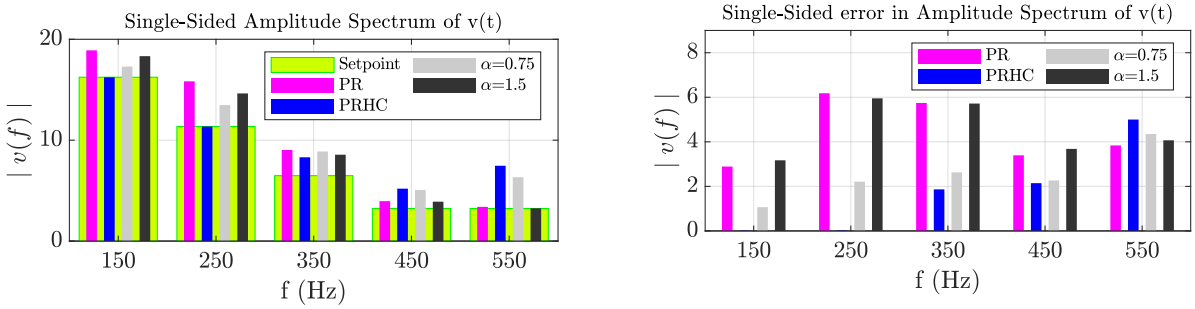

(**a**) Spectrum of tracking signal (**b**) Spectrum of tracking error

Figure 16. FFT for the tracking voltage time response in Figure 15.

5.2. Non-Linear Load (Disturbance)

A single-phase non-linear load is connected to the VC-VSC, consisting of a series resistor of 1 Ω followed by a diode bridge with a 22 Ω resistor and a 2.2 mF capacitor in parallel (based on IEC-62040-3 Annex E [38]. The load current total harmonic distortion (THD) is 101.5%. For this case, the controllers include a feedforward compensator.

The results of the disturbance rejection are depicted in Figure 17. Due to the nature of the non-linear load proposed, the voltage control loop needs to respond fast every half

period of the voltage fundamental component reference. This is reflected in Figure 17 where the PRHC controller and FPR with α equal to 0.75 show the best time evolution.

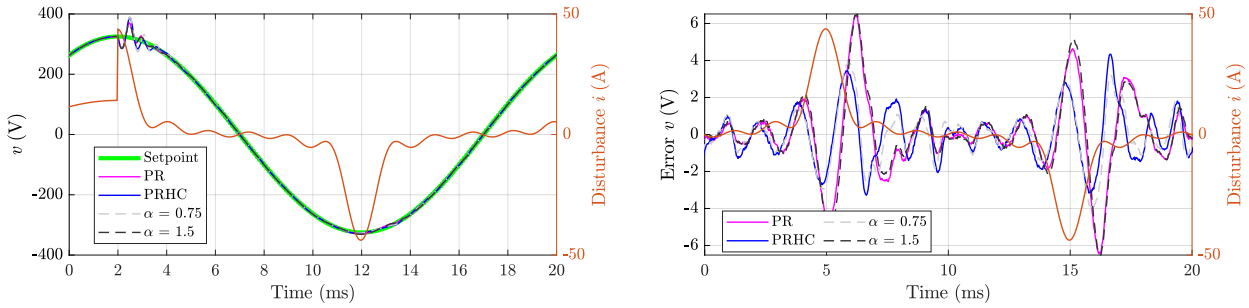

(**a**) Voltage tracking

(**b**) Voltage tracking error at steady−state

Figure 17. Disturbance rejection time response. The orange line in the right figure depicts the disturbance on the tracking error plot.

Table 7 provides specific values and highlights the best option for each component. The voltage tracking transient and the error response are depicted when the non-linear load is connected.

Table 7. Multi-harmonic disturbance response and total voltage THD content for all four controllers.

Controller	V_{150Hz} (V/A)	V_{250Hz} (V/A)	V_{350Hz} (V/A)	V_{450Hz} (V/A)	V_{550Hz} (V/A)	THD (%)
PR	0.035	0.0127	0.290	0.433	0.402	0.95
PRHC	**0**	**0**	**0.092**	**0.265**	0.443	**0.71**
α = 0.75	0.010	0.052	0.133	0.280	**0.372**	**0.71**
α = 1.5	0.0130	0.125	0.294	0.456	0.424	0.97

Bold values indicate the best option.

The FFT for the disturbance and the voltage error are computed; see Figure 18. The FFTs show the FPR with α = 0.75 starts to be better at high frequencies.

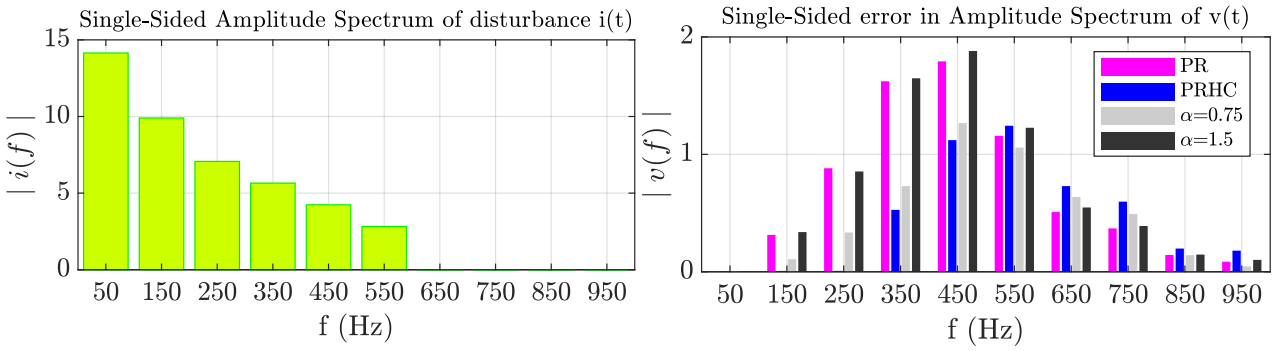

(**a**) Spectrum of disturbance signal

(**b**) Spectrum of disturbance error

Figure 18. FFT for steady-state disturbance rejection in Figure 17.

5.3. DSP Implementation Comparison

This section compares the controllers used across the experimental implementation regarding computation burdens. The two following criteria are used: execution time and program memory.

Table 8 collects the obtained results. From Section 3 it should be noted that the FPR controller approximation for α = 0.75 uses an order approximation of 2, while when α is set to 1.5, it uses order 3.

Table 8. Controller type comparison. Execution time and program memory data.

Controller Type	Execution Time (µs)	Program Memory (Bytes)
PR	0.321	85
PRHC (3 HC)	0.788	141
FPR ($\alpha = 0.75$)	0.802	116
FPR ($\alpha = 1.5$)	0.913	134

From Table 8, it can be seen that the FPR arises as one outstanding controller for covering a wide bandwidth of controlled frequencies and improving the rejection capability over other classical options such as PR or PRHC. Therefore, any advanced low-order controller, like the proposed FPR controller for voltage-controlled applications, can reduce execution time, allowing the saved time to be allocated to other critical tasks, such as generating real-time alarms.

6. Discussion

This section summarises the results from previous sections.

The application addressed by the FPR controller is framed considering a VC-VSC with an output LC coupling filter. The control scheme is then based on two nested control loops, assuming the inner loop is negligible for the stability analysis. The defined range of the fractal component is $\alpha \in (0, 2]$, considering only causal implementation forms of the controller.

Firstly, using classical techniques such as the Nyquist criterion allows to face the stability challenge. The Nyquist trajectories analysis concludes that α values above 1 hold system stability. On the contrary, decreasing α under 1 must be cautiously performed to avoid instabilities. This permits us to deduce that the FPR controller on voltage-controlled application can be valid if α is well selected.

Secondly, considering a tuning procedure to obtain a specific gain margin allows to compare different controllers with the FPR controller for voltage applications. Under this assumption, the sensitivity analysis conclusion is that FPRs with α values below 1 present a better phase delay tracking and disturbance rejection. This statement should be considered valid when the same phase margin at a specific frequency is used as a tuning criterion. On the contrary, α values above 1 result in the opposite but present lower undesired amplification gains and accomplish better robustness and stability margins. Thirdly, compared to traditional control methods such as PR controllers, fractional tuning of certain parameters can enhance tracking accuracy, decrease phase delay, and improve disturbance rejection. However, fractional-order proportional (FPR) controllers add extra parameters due to their fractional-order elements, increasing the complexity of the tuning process. Optimally selecting these fractional parameters can be challenging, particularly when balancing performance with stability and robustness. In this direction, implementing the FPR on a processor will require analysis of the discretisation procedure to ensure a proper correspondence between the continuous and the discrete-time domain, paying special attention to the sampling time and discretisation strategy used.

Finally, ideal PRHC controllers (no damping or phase margin compensation) could have better tracking capabilities for individual tones. However, it is at the cost of potentially worsening the interharmonic control, lessening the stability and robustness margins, and increasing computational burdens when a wide range of frequencies want to be controlled.

The spider diagram depicted in Figure 19 helps to rapidly compare the proposed FPR with the PR or PRHC alternatives according to the relevant points studied: execution time, stability, disturbance rejection, controllability and complexity.

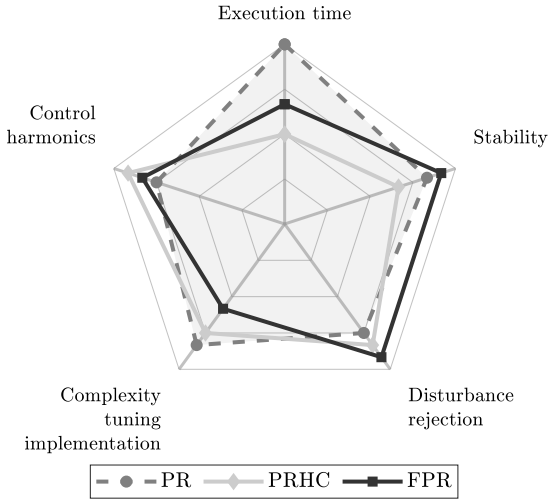

Figure 19. Controller type comparison (the closer to the peak, the better the result).

7. Conclusions

This paper proposes to use fractional proportional–resonant (FPR) controllers for AC voltage regulation.

The paper analyses the stability through the Nyquist trajectory conceptualisation applied to the continuous-time domain. This stability study concludes that if the stability of the fractional term in the range $\alpha \in [1, 2]$ is not compromised, while if α is lower than 1, it could be according to the selected fractional term and the system parameters.

The paper proposes a methodology to obtain the FPR controllers' gains. The methodology derives analytical expressions that can be used to set a specific gain margin at a specific frequency.

An in-depth analysis of the proposed formulation when using the tuning proposal was conducted, focusing on the challenges of sensitivity and robustness. This analysis was performed by comparing FPR controllers with classical proportional–resonant (PR) controllers that include harmonic compensators (HC). A consistent tuning method was applied as a common criterion alongside sensitivity analysis to establish a comparable framework for evaluating the controllers' performance. The findings indicate that the FPR controller maintains validity without significant negative impacts on sensitivity and robustness. This approach was validated through simulations and experimental tests, which demonstrate that the FPR controller can be effectively designed to enhance various control objectives, including frequency tracking of AC voltage references and increased system stability and robustness against inaccuracies.

Therefore, the FPR controller emerges as a good alternative to multi-harmonic proportional resonant controllers with a contained implementation. Furthermore, the FPR controller stands out above for applications in which controlling the AC voltage and rejecting load disturbances is a key factor, such as grid-forming converters or AC power supplies.

Author Contributions: Conceptualisation, D.H.-P.; methodology, D.H.-P., D.M.-M. and J.M.-F.; software, C.C.-A. and T.L.-P.; validation, D.H.-P., C.C.-A. and D.M.-M.; formal analysis, D.H.-P. and J.M.-F.; investigation, D.H.-P. and T.L.-P.; data curation, C.C.-A.; writing—original draft preparation, D.H.-P.; writing—review and editing, D.H.-P., D.M.-M., C.C.-A., T.L.-P. and J.M.-F.; supervision, J.M.-F. All authors have read and agreed to the published version of the manuscript.

Funding: This research received no external funding.

Institutional Review Board Statement: Not applicable.

Informed Consent Statement: Not applicable.

Data Availability Statement: Data is contained within the article.

Conflicts of Interest: The authors declare no conflicts of interest.

Abbreviations

The following abbreviations are used in this manuscript:

AC	Alternative Current
ESR	Equivalent Series Resistance
FOC	Fractional Order Calculus
FPR	Fractional–Proportional–Resonant
GM	Gain Margin
HC	Harmonic Compensator
IMC	Internal Model Control
PI	Proportional–Integral
PID	Proporional–Integral–Derivative
PIHC	Proportional–Integral with Harmonic Compensator
PM	Phase Margin
PR	Proportional–Resonant
PRHC	Proportional–Resonant with Harmonic Compensator
PSO	Particle Swarm Optimisation
VC	Voltage Controlled
VSC	Voltage Source Converter

References

1. Monter, A.R.; Bueno, E.J.; García-Cerrada, A.; Rodríguez, F.J.; Sánchez, F.M. Detailed analysis of the implementation of frequency-adaptive resonant and repetitive current controllers for grid-connected converters. *Electr. Power Syst. Res.* **2014**, *116*, 231–242. [CrossRef]
2. Quan, X.; Dou, X.; Wu, Z.; Hu, M.; Yuan, J. Harmonic voltage resonant compensation control of a three-phase inverter for battery energy storage systems applied in isolated microgrid. *Electr. Power Syst. Res.* **2016**, *131*, 205–217. [CrossRef]
3. Zammit, D.; Apap, M. Comparison between PI and PR Current Controllers in Grid Connected PV Inverters. *Int. J. Electr. Electron. Sci. Eng.* **2014**, *8*, 221–226.
4. Yepes, A.G.; Freijedo, F.D.; Doval-Gandoy, J.; López, O.; Malvar, J.; Fernández-Comesaña, P. Effects of discretization methods on the performance of resonant controllers. *IEEE Trans. Power Electron.* **2010**, *25*, 1692–1712. [CrossRef]
5. Lascu, C.; Asiminoaei, L.; Boldea, I.; Blaabjerg, F. High-performance current controller for selective harmonic compensation in active power filters. *IEEE Trans. Power Electron.* **2007**, *22*, 1826–1835. [CrossRef]
6. Hans, F.; Schumacher, W.; Chou, S.F.; Wang, X. Design of Multifrequency Proportional–Resonant Current Controllers for Voltage-Source Converters. *IEEE Trans. Power Electron.* **2020**, *35*, 13573–13589. [CrossRef]
7. Yepes, A.G.; Freijedo, F.D.; López, O.; Doval-Gandoy, J. High-performance digital resonant controllers implemented with two integrators. *IEEE Trans. Power Electron.* **2011**, *26*, 563–576. [CrossRef]
8. Xie, B.; Guo, K.; Mao, M.; Zhou, L.; Liu, T.; Zhang, Q.; Hao, G. Analysis and Improved Design of Phase Compensated Proportional Resonant Controllers for Grid-Connected Inverters in Weak Grid. *IEEE Trans. Energy Convers.* **2020**, *35*, 1453–1464. [CrossRef]
9. Ebrahim, M.A.; Aziz, B.A.; Nashed, M.N.; Osman, F. Optimal design of controllers and harmonic compensators for three-level cascaded control in stationary reference frame for grid-supporting inverters-based AC microgrid. *Energy Rep.* **2022**, *8*, 860–877. [CrossRef]
10. Bingi, K.; Kulkarni, R.R.; Mantri, R. Design and Analysis of Complex Fractional-order PID Controllers. In Proceedings of the 2021 IEEE Madras Section Conference (MASCON), Chennai, India, 27–28 August 2021; pp. 1–6. [CrossRef]
11. Caponetto, R.; Maione, G.; Sabatier, J. Fractional-order control: A new approach for industrial applications. *Control Eng. Pract.* **2016**, *56*, 157–158. [CrossRef]
12. Azghandi, M.A.; Barakati, S.M.; Yazdani, A. Impedance-Based Stability Analysis and Design of a Fractional-Order Active Damper for Grid-Connected Current-Source Inverters. *IEEE Trans. Sustain. Energy* **2021**, *12*, 599–611. [CrossRef]
13. Kumar, A.; Pan, S. Design of fractional order PID controller for load frequency control system with communication delay. *ISA Trans.* **2022**, *129*, 138–149. [CrossRef] [PubMed]
14. Podlubny, I. Fractional-order systems and PI-lambda-D-mu controllers. *IEEE Trans. Autom. Control* **1999**, *44*, 208–214. [CrossRef]
15. Shah, P.; Agashe, S. Review of fractional PID controller. *Mechatronics* **2016**, *38*, 29–41. [CrossRef]
16. Heredero-Peris, D.; Chillón-Antón, C.; Sánchez-Sánchez, E.; Montesinos-Miracle, D. Fractional proportional-resonant current controllers for voltage source converters. *Electr. Power Syst. Res.* **2019**, *168*, 20–45. [CrossRef]
17. Abdulwahhab, O.W. Design of a Complex fractional Order PID controller for a First Order Plus Time Delay system. *ISA Trans.* **2020**, *99*, 154–158. [CrossRef]

18. Zheng, W.; Luo, Y.; Chen, Y.; Wang, X. Synthesis of fractional order robust controller based on Bode's ideas. *ISA Trans.* **2021**, *111*, 290–301. [CrossRef]
19. Zafari, A.; Mehrasa, M.; Bacha, S.; Al-Haddad, K.; Hosseinzadeh, N. A Robust Fractional-Order Control Technique for Stable Performance of Multilevel Converter-Based Grid-Tied DG Units. *IEEE Trans. Ind. Electron.* **2022**, *69*, 10192–10201. [CrossRef]
20. Li, M.; Li, D.; Wang, J.; Zhao, C. Active disturbance rejection control for fractional-order system. *ISA Trans.* **2013**, *52*, 365–374. [CrossRef]
21. De Keyser, R.; Muresan, C.I.; Ionescu, C.M. A novel auto-tuning method for fractional order PI/PD controllers. *ISA Trans.* **2016**, *62*, 268–275. [CrossRef]
22. Malek, H.; Dadras, S.; Yin, C.; Chen, Y. Fractional Order Proportional-Resonant Controller. In Proceedings of the 2018 Annual American Control Conference (ACC), Milwaukee, WI, USA, 27–29 June 2018; pp. 3086–3091. [CrossRef]
23. Heredero-Peris, D.; Sánchez-Sánchez, E.; Chillón-Antón, C.; Montesinos-Miracle, D.; Gálceran-Arelláno, S. A novel fractional proportional-resonant current controller for voltage source converters. In Proceedings of the 2016 18th European Conference on Power Electronics and Applications (EPE'16 ECCE Europe), Karlsruhe, Germany, 5–9 September 2016; pp. 1–10.
24. Haro-Larrode, M.; Bergna-Diaz, G.; Eguia, P.; Santos-Mugica, M. On the Tuning of Fractional Order Resonant Controllers for a Voltage Source Converter in a Weak AC Grid Context. *IEEE Access* **2021**, *9*, 52741–52758. [CrossRef]
25. Sahu, J.; Satapathy, P.; Debnath, M.K.; Mohanty, P.K.; Sahu, B.K.; Padhi, J.R. Automatic voltage regulator design based on fractional calculus plus PID controller. In Proceedings of the 2020 International Conference on Computational Intelligence for Smart Power System and Sustainable Energy (CISPSSE), Keonjhar, Odisha, India, 29–31 July 2020; pp. 1–4. [CrossRef]
26. Trivedi, R.; Padhy, P.K. Design of Indirect Fractional Order IMC Controller for Fractional Order Processes. *IEEE Trans. Circuits Syst. II: Express Briefs* **2021**, *68*, 968–972. [CrossRef]
27. Idir, A.; Akroum, H.; Tadjer, S.A.; Canale, L. A Comparative Study of Integer Order PID, Fractionalized Order PID and Fractional order PID Controllers on a Class of Stable System. In Proceedings of the 2023 IEEE International Conference on Environment and Electrical Engineering and 2023 IEEE Industrial and Commercial Power Systems Europe (EEEIC / ICPS Europe), Madrid, Spain, 6–9 June 2023; pp. 1–6. [CrossRef]
28. Amini, B.; Roshanfekr, R.; Hajipoor, A.; Mousazadeh Mousavi, S.Y. Interface converter control of distributed generation in microgrids using fractional proportional—Resonant controller. *Electr. Power Syst. Res.* **2021**, *194*, 107097. [CrossRef]
29. Matignon, D. Stability Results For Fractional Differential Equations With Applications To Control Processing. *Comput. Eng. Syst. Appl.* **1997**, *2*, 963.
30. Zhou, Y.; Miao, Z.; Li, Y.; Fan, L. Design robust cascade control structure for voltage source converters. In Proceedings of the 2017 North American Power Symposium (NAPS), Morgantown, WV, USA, 17–19 September 2017.
31. Monje, C.; Chen, Y.; Vinagre, B.; Xue, D.; Feliu, V. *Fractional Order Systems and Control - Fundamentals and Applications*; Springer: Berlin/Heidelberg, Germany, 2010. [CrossRef]
32. Charef, A.; Sun, H.; Tsao, Y.; Onaral, B. Fractal system as represented by singularity function. *IEEE Trans. Autom. Control* **1992**, *37*, 1465–1470. [CrossRef]
33. Vinagre, B.M.; Podlubny, I.; Hernández, A.; Feliu, V. Some approximations of fractional order operators used in control theory and applications. *Fract. Calc. Appl. Anal.* **2000**, *3*, 231–248.
34. Oustaloup, A.; Levron, F.; Mathieu, B.; Nanot, F. Frequency-band complex noninteger differentiator characterization and synthesis. *IEEE Trans. Circuits Syst. I: Fundam. Theory Appl.* **2000**, *47*, 25–39. [CrossRef]
35. Åström, K.J.; Murray, R.M. *Feedback Systems: An Introduction for Scientists and Engineers*; Princeton University Press: Princeton, NJ, USA, 2010; Volume 5.
36. Hušek, P. PID controller design for hydraulic turbine based on sensitivity margin specifications. *Int. J. Electr. Power Energy Syst.* **2014**, *55*, 460–466. [CrossRef]
37. Goodwin, G.C.; Graebe, S.F.; Salgado, M.E. *Control System Design*; Prentice Hall: Upper Saddle River, NJ, USA, 2000.
38. *IEC 62040-3*; Uninterruptible Power Systems (UPS)—Part 3: Method of Specifying the Performance and Test Requirements. International Electrotechnical Commission: Geneva, Switzerland, 2021.